J. Mol. Biol. (1994) **742**, 683–700

Towards Atomic Interpretation of F-Actin Filament Three-dimensional Reconstructions

A. Bremer[1,2], C. Henn[1], K. N. Goldie[1], A. Engel[1], P. R. Smith[3] and U. Aebi[1,4]

[1]*M.E. Müller-Institute for Microscopy at the Biozentrum University of Basel, CH-4056 Basel, Switzerland*

[2]*Department of Cell Biology Duke University Medical Center, Durham, NC 27710, U.S.A.*

[3]*Department of Cell Biology New York University Medical Center, New York, NY 10016, U.S.A.*

[4]*Department of Cell Biology and Anatomy The Johns Hopkins University School of Medicine, Baltimore, MD 21205, U.S.A.*

We have recorded dark field images of negatively stained F-actin filaments polymerized with 2 mM $MgCl_2$ and 50 mM KCl with a scanning transmission electron microscope and computed 3-D reconstructions using a helical parameter search to optimize simultaneously the helical repeat length, the radial position of the filament axis, and the helical selection rule. The resulting optimized averaged filament 3-D reconstruction at 2·5 nm resolution is remarkably similar to an atomic model of the F-actin filament. By comparison, several structural features of the reconstruction can be interpreted at the level of distinct secondary structure elements, and predictions made by the atomic model could be verified: for instance, the density connecting the two long-pitch helical strands in our reconstruction co-localizes with an extended β-hairpin, the "hydrophobic loop" (i.e. residues 262 to 274), which according to the atomic model establishes the major intersubunit contact between the two long-pitch helical strands. The most pronounced structural variations among individual filament 3-D reconstructions were observed in (1) the details of the intersubunit contact pattern between the two long-pitch helical strands, and (2) the exact size and shape of subdomain 2 of the F-actin molecule, which appears rather flexible and easily deformed. In addition, we found that all phenotypes of F-actin filament 3-D reconstructions that arise from small deviations from the optimal helical parameters or from lowering the nominal resolution exhibited stronger intersubunit contacts between than along the two long-pitch helical strands, a structural feature that has been emphasized for a number of F-actin filament 3-D reconstructions in the past. Since this is clearly at variance with the relative strength of the intersubunit contacts as predicted by the atomic model, it may represent an artifactual structural feature arising from low-resolution data or suboptimal helical data processing, and should therefore be interpreted with caution in terms of indicating chemical, mechanical or conformational states of the F-actin filament.

Keywords: F-actin filament; electron microscopy; negative staining; three-dimensional reconstruction; molecular modelling

1. Introduction

Actin filaments serve as railroad tracks for the eukaryotic protein machinery that drives muscle contraction, cell motility, cytokinesis, and other active changes of the cell shape (Herman, 1993; Reisler, 1993; Bray, 1992; Kabsch & Vandekerckhove, 1992). The 43 kDa G-actin monomer that can be isolated from muscle and non-muscle sources at low ionic strength (e.g. 0·2 mM $CaCl_2$ or $MgCl_2$) typically consists of 375 amino acid residues. Under physiologically relevant salt concentrations (e.g. 2 mM $MgCl_2$ and 50 mM KCl), G-actin rapidly polymerizes by a helical nucleation-condensation mechanism (Oosawa & Kasai, 1962; for a review, see Carlier, 1991) into F-actin filaments that can become several micrometers long. The filament consists of two

† Correspondence: Ueli Aebi, M.E. Müller-Institute for Microscopy at the Biozentrum, Klingelbergstrasse 70, CH-4056 Basel, Switzerland.

0022-2836/94/400683-18 $08.00/0

long-pitch helical strands of subunits that have the same polarity and are axially staggered by 2·75 nm, exactly half the length of one actin subunit when measured in the direction of the filament axis. An alternative description of the filament structure is a so-called "genetic" helix with six left-handed turns per 13 subunits. The intersubunit contacts along the two long-pitch helical strands are approximately three times stronger than between them (for a review, see Bremer & Aebi, 1992). Therefore, the two long-pitch helical strands can move relatively independent of each other by "lateral slipping" (Bremer *et al.*, 1991; Censullo & Cheung, 1993).

Helical 3-D† reconstruction was developed more than a quarter of a century ago (Klug & DeRosier, 1966) and became an extraordinarily powerful tool to elucidate the 3-D structure of many supramolecular assemblies (for a review, see Stewart, 1988). Tobacco mosaic virus, TMV, was a particularly rewarding specimen: 3-D reconstructions at 1·0 nm resolution were computed from images of negatively stained (Unwin & Klug, 1974) and, 15 years later, frozen-hydrated preparations (Jeng *et al.*, 1989). The structure of TMV was also solved to atomic resolution by X-ray crystallography (Namba & Stubbs, 1986). By contrast, the highest resolution so far achieved with dispersed F-actin filaments is much lower, only about 2·8 nm (Bremer *et al.*, 1991, 1992). The intrinsic structural dynamics and flexibility of the F-actin filament and its subunits appear to limit the achievable resolution, since local deviations from perfect helical symmetry (e.g. local unraveling because of lateral slipping) cannot be corrected for easily by image processing and reconstruction.

The structure of the actin molecule in complex with the actin-binding proteins DNase I (Kabsch *et al.*, 1990), gelsolin segment I (McLaughlin *et al.*, 1993) and profilin (Schutt *et al.*, 1993) has been solved to atomic resolution by X-ray crystallography. Accordingly, the molecule measures about 5·5 nm × 5·5 nm × 3·5 nm and is composed of two domains termed large and small (Kabsch *et al.*, 1990). These two domains can each be subdivided further into two subdomains each (for a review, see Holmes *et al.*, 1993). Starting from the atomic coordinates (Kabsch *et al.*, 1990), Holmes and co-workers have constructed and refined atomic models of the actin filament that fit X-ray fiber diffraction data of oriented F-actin gels (Holmes *et al.*, 1990; Lorenz *et al.*, 1993).

We have optimized our EM data acquisition and image reconstruction strategy and the resulting optimized F-actin filament 3-D reconstructions are remarkably similar to the atomic filament models. This prompted us to explore whether EM data at a nominal resolution of 2·5 nm can reliably evaluate, i.e. verify or falsify, atomic models of the actin filament. The structure of the myosin subfragment-1 (S-1) has recently been solved to atomic resolution (Rayment *et al.*, 1993*a*) but high-resolution X-ray fiber diffraction patterns of S-1-decorated F-actin filaments may be difficult to obtain. Reaching a consensus on the atomic structure of the F-actin filament between X-ray crystallography, molecular modelling and electron microscopy could therefore become a paradigm for structural research in the field of muscle proteins, since developing detailed molecular or even atomic models for the interaction between actin and S-1 may depend heavily on high-resolution EM data (Rayment *et al.*, 1993*b*; Schröder *et al.*, 1993).

In several recently published actin filament reconstructions (Bremer *et al.*, 1991; Bremer & Aebi, 1992; Lepault *et al.*, 1994; Orlova & Egelman, 1992, 1993; Owen & DeRosier, 1993; Schmid *et al.*, 1994), structural differences among 3-D reconstructions or relative to the atomic models by Holmes and co-workers (Holmes *et al.*, 1990; Lorenz *et al.*, 1993) were observed. The question whether these differences represent real distinct chemical, mechanical or conformational states or whether they are produced by different effective resolutions or suboptimal processing of the filament data that are compared has thus far received little if any attention. To provide a more solid basis for evaluating the significance of observed structural differences, we have systematically analyzed the phenotypes of low-resolution and suboptimally processed F-actin filament 3-D reconstructions.

2. Materials and Methods

(a) *Materials*

All chemicals used were at least of reagent grade, mostly of analytical or best available grade. ATP (A-2383, sodium salt, grade I) was purchased from Sigma Chemical Corporation (St. Louis, MO). Uranyl formate was obtained from BDH Chemicals Ltd (Poole, England). For all experiments, water deionized by a Skan NANOpure cartridge system (Skan AG, Basel-Allschwil, Switzerland) with a specific residual resistivity of better than 18 MΩ cm was used. The only exception was that we washed the grids for STEM imaging (200 mesh/inch copper grids coated with reticulated carbon support films) with double-distilled water after sample adsorption (see below). Electron image film SO-163 and developer D-19 were products of Eastman Kodak (Rochester, NY).

(b) *Preparation of G-actin*

Unless stated otherwise, all manipulations were carried out at 4°C. Actin was isolated by a modification of a previously described protocol (Millonig *et al.*, 1988). Briefly, rabbit skeletal muscle acetone powders were extracted twice with 40 ml of Mg-ATP buffer G (2·0 mM imidazole, 0·2 mM $MgCl_2$, 0·2 mM ATP, 0·5 mM DTT, pH 7·4 at 4°C) per gram of powder for 30 minutes. The pooled and filtered

†Abbreviations used: 2-D and 3-D, two- and three-dimensional; G-actin, monomeric actin; F-actin, filamentous actin; EM, electron microscope/microscopy; CTEM, conventional transmission electron microscope/microscopy; STEM, scanning transmission electron microscope/microscopy; ADF, annular dark field; DNase I, bovine pancreatic deoxyribonuclease I; TMV, tobacco mosaic virus; CPK, Corey-Pauling-Koltun; S-1, myosin subfragment-1.

low-speed supernatants (27,500 *g* for 30 minutes) were polymerized for 30 minutes at room temperature by addition of KCl to 50 mM and $MgCl_2$ to 2 mM, followed by an additional 30 minutes on ice. Solid KCl was then added to a final concentration of 0·8 M and the polymerized solution was stirred slowly for 60 minutes. The polymerized material was pelleted at 100,000 *g* for two hours. The pellet was resuspended in 20 ml of Ca-ATP buffer A (2·5 mM imidazole, 0·2 mM $CaCl_2$, 0·2 mM ATP, 0·005% (w/v) sodium azide, 0·1 mM DTT, pH 7·4 at 4°C). After dialysis against this buffer for three days with buffer changes every day, the depolymerized actin was clarified by centrifugation at 125,000 *g* for two hours. The upper two-thirds of the resulting supernatant, typically 12 to 15 ml, was adjusted to a protein concentration of 6 to 8 mg/ml and gel-filtered on a 2·6 cm diameter Sephadex G-200 gel filtration column with an effective gel bed length of approximately 1 m. The resulting G-actin peak fractions were stored in Ca-ATP buffer A and used within one to two weeks. Using Mg^{2+} instead of Ca^{2+} as the divalent cation in the extraction from acetone powders significantly attenuated actin proteolysis by endogenous, seemingly Ca^{2+}-dependent proteases as judged by SDS-PAGE.

(c) *Polymerization of G-actin into F-actin filaments*

F-Actin filaments were polymerized at room temperature for 60 minutes from G-actin at a protein concentration of 1 mg/ml by adding $MgCl_2$ to 2 mM and KCl to 50 mM.

(d) *Specimen preparation, electron microscopy and data acquisition*

F-Actin filaments were pelleted by centrifugation for 15 minutes at 100,000 *g* and resuspended in the original volume of polymerization buffer (i.e. Ca-ATP buffer A supplemented with 2 mM $MgCl_2$ and 50 mM KCl). The resuspended material was then diluted with polymerization buffer to yield a protein concentration of 0·2 mg/ml, immediately adsorbed to copper grids coated with reticulated carbon support films, and negatively stained with 0·75% (w/v) uranyl formate (pH 4·25), as described (Bremer & Aebi, 1994). Scanning transmission electron microscopy (STEM) was performed using a Vacuum Generators (East Grinstead, England) STEM HB5 operated at an acceleration voltage of 80 kV. The electron doses were 10^3 e^-/nm^2 at a nominal magnification of 200,000 ×, or 5×10^3 e^-/nm^2 at a nominal magnification of 500,000 ×. Annular dark field (ADF) micrographs were recorded in digital format by a custom-built data acquisition system (Müller *et al.*, 1992). The frame size of 512 × 512 pixels corresponded to a pixel size of 0·9 nm (nominal magnification 200,000 ×) or 0·36 nm (nominal magnification 500,000 ×). Preparation of specimens for conventional transmission electron microscopy (CTEM), recording CTEM images and digitizing them was performed as described (Bremer *et al.*, 1991).

(e) *Digital image reconstruction*

We selected uniformly stained, relatively straight filament stretches with evenly spaced crossovers and well-resolved subunits (see Figure 1) for digital image reconstruction. First, the filament axis was defined by fitting a cubic spline through peaks in averaged cross-correlation maps of the filament image with at least three independent references extracted from the image itself. The filament axis thus defined was refined interactively and orthogonalized by bilinear interpolation along equidistant normals. The helical parameters (i.e. the length of the helical repeat, the radial coordinate of the filament axis and the helical selection rule) of such unbent filament stretches were then optimized as detailed in Results. The F-actin filament image array was always interpolated to an axial length of ten times the number of subunits in the assumed helical repeat (e.g. 130 pixels for the helical selection rule $l = -6n + 13m$) before $D(Z, k)$-filtration (Smith & Aebi, 1974). This sampling corresponds to a pixel size of 0·275 nm assuming 5·5 nm as the axial repeat of the subunits along the two long-pitch helical strands. The array width was always trimmed to 56 pixels, corresponding to $56 \times 0{\cdot}275$ nm = 15·4 nm. After $D(Z, k)$-filtration, unless stated otherwise, filament transforms were isotropically limited in their resolution to nominally 2·5 nm by multiplication with a circular mask with Gaussian edges (S.D. 0·5 nm). All the filament images were finally reinterpolated to the helical selection rule $l = -6n + 13m$, and the equator, the 1st, 2nd, 5th, 6th, 7th, 8th, 13th, and 14th layerline were extracted. Most digital image reconstruction was done using the micrograph data processing program MDPP (Smith, 1978). Filament unbending and limiting the resolution was done using the SEMPER image processing package (Saxton & Baumeister, 1982). These program packages were run on a DEC VAX server 4000-300 or a DEC VAX workstation 4000-60.

(f) *Averaging of reconstructed images*

For averaging, we oriented helical repeats following the conventions of Holmes and co-workers (Holmes *et al.*, 1990) with the "pointed end" of the filament with regards to the S-1 decoration pattern pointing up. Our criterion for this orientation was that the "mini-arrowhead" pattern (Bremer *et al.*, 1991) observed in $D(Z, k)$-filtered filament images pointed down. Averaging five to 15 reconstructions required about three to five cycles of an iterative alignment procedure to obtain stable parameters for rotational and translational alignment: $D(Z, k)$-transforms were aligned by layerline correlation with a reference, backtransformed and added with equal weight after normalizing them to the same mean and standard deviation to produce a new reference. The initial reference was a previous 2-D reconstruction (Bremer *et al.*, 1992). The program for layerline correlation (Smith *et al.*, 1976) worked in two steps. A first correlation determined the approximate alignment parameters (search radius: angularly over 360° in 2° steps, axially over one helical repeat in 0·015-helical-repeat steps). These parameters served as the origin for refinement (search radius: angularly over 36° in 0·05° steps, axially over 0·2 helical repeats in 0·001-helical-repeat steps).

(g) *Helical 3-D reconstructions, model building and visualization*

We computed 3-D reconstructions (DeRosier & Moore, 1970; Smith *et al.*, 1976) as stacks of 0·275 nm spaced vertical sections, each 56 by 56 pixels (i.e. 15·4 nm × 15·4 nm) wide. Solid-rendered, reflection-mapped isosurfaces were generated from these image stacks using the program MapView that was developed by one of us (C.H.) and implements real-time solid contouring based on the "marching cube" concept (Lorenzen & Cline, 1987). Contouring levels to include predetermined fractions of the nominal molecular volume of the 42 kDa actin subunit as indicated in the text were computed using histogram integration assuming a hydrated protein density of

0·81 Da/Å^3 (Taylor & Amos, 1981). Triangle coordinate files for ribbon drawings were created using a customized version of Ribbons 2·0 (Carson, 1987). Ray-traced CPK representations were generated with the Raster3D Tools (developed by D. Bakon and W. Anderson, 1988). All other ray-tracing was done using RayShade 4·0 (developed by C. E. Kolb and R. Bogart, 1991) with coordinate files generated in MapView and Ribbons 3·0. All visualization programs were run on a Silicon Graphics Crimson with 64 MByte RAM, equipped with a Reality Engine graphics subsystem. All programs used were customized to take advantage of the advanced graphics features (i.e. full-scene antialiasing, 64-fold multisampling).

3. Results

(a) *Processing F-acting filament stretches*

A STEM ADF image of negatively stained F-actin filaments recorded at a nominal magnification of 200,000 × is shown in Figure 1a. For helical processing, we used images as shown in Figure 1b that were recorded at a nominal magnification of 500,000 ×. From more than 100 filament images selected according to our criteria (see Materials and Methods), about 50% had to be rejected during digital unbending because their filament axis could not be traced unambiguously. Approximately another 50% of the remaining filaments was not of sufficient quality to be processed with selection rules that required three or more crossovers. In a 3-D helical parameter search, the unbent filament images were optimized for their helical repeat length, the radial position of the filament axis, and the helical selection rule. The ten filament stretches with the highest transmitted power upon $D(Z, k)$-filtration (Smith & Aebi, 1974) were selected for further processing (see below). Figure 2a demonstrates for one of these ten filaments how the power transmitted upon $D(Z, k)$-filtration depends on the radial position of the filament axis and on the assumed helical repeat length. Whereas the transmitted power changes dramatically with the radial coordinate of the filament axis, it is less sensitive to variations in the assumed helical repeat length. We always observed an absolute maximum that could be located unambiguously by a computational peak search (see intersection of the 3-D plot with the horizontal plane).

In the 3-D helical parameter search, the following helical selection rules $l = un + vm$ were tested: $l = -11n + 24m$ (screw angle ψ between adjacent subunits along the genetic helix: $\psi = -165{\cdot}00°$; averaging over two helical repeats); $l = -6n + 13m$ ($\psi = -166{\cdot}15°$; averaging over three helical repeats); $l = -19n + 41m$ ($\psi = -166{\cdot}83°$; averaging over one helical repeat); $l = -13n + 28m$ ($\psi = -167{\cdot}14°$; averaging over two helical repeats); $l = -20n + 43m$ ($\psi = -167{\cdot}44°$; averaging over one helical repeat); $l = -7n + 15m$ ($\psi = -168{\cdot}00°$; averaging over three helical repeats); $l = -22n + 47m$ ($\psi = -168{\cdot}51°$; averaging over one helical repeat); $l = -25n + 53m$ ($\psi = -169{\cdot}81°$; averaging over one helical repeat); and $l = -9n + 19m$ ($\psi = -170{\cdot}53°$; averaging over two helical repeats). Since the $D(Z, k)$-filtration eliminates the noise that is incompatible with the assumed helical symmetry, the power transmitted upon $D(Z, k)$-filtration depends on how well the transformed structure matches the assumed helical selection rule. In addition, the transmitted power depends on the number of axially repeating units (i.e. "helix segments" that are proportional to the number of subunits) included in the $D(Z, k)$-transform. To demonstrate how the transmitted power depends on

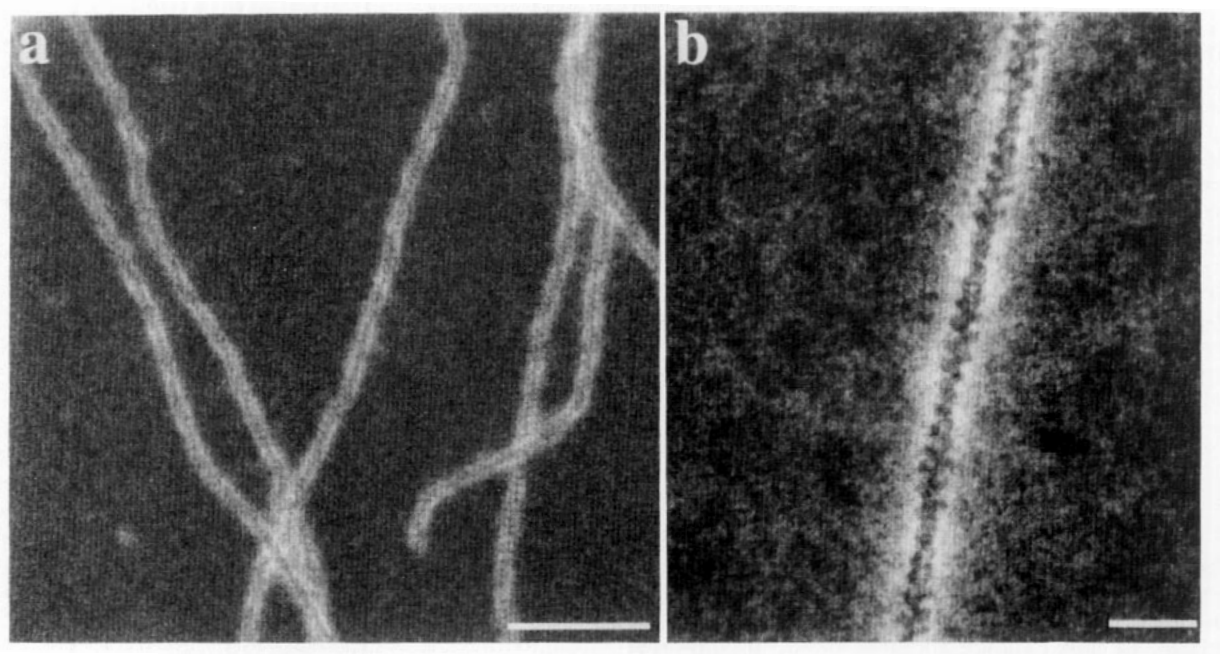

Figure 1. Negatively stained F-actin filaments. F-actin filaments polymerized for 60 min at room temperature with 2 mM $MgCl_2$ and 50 mM KCl have been imaged at a nominal magnification of (a) 200,000 × and (b) 500,000 × in a STEM using the ADF detector. The scale bars represent (a) 100 nm and (b) 20 nm.

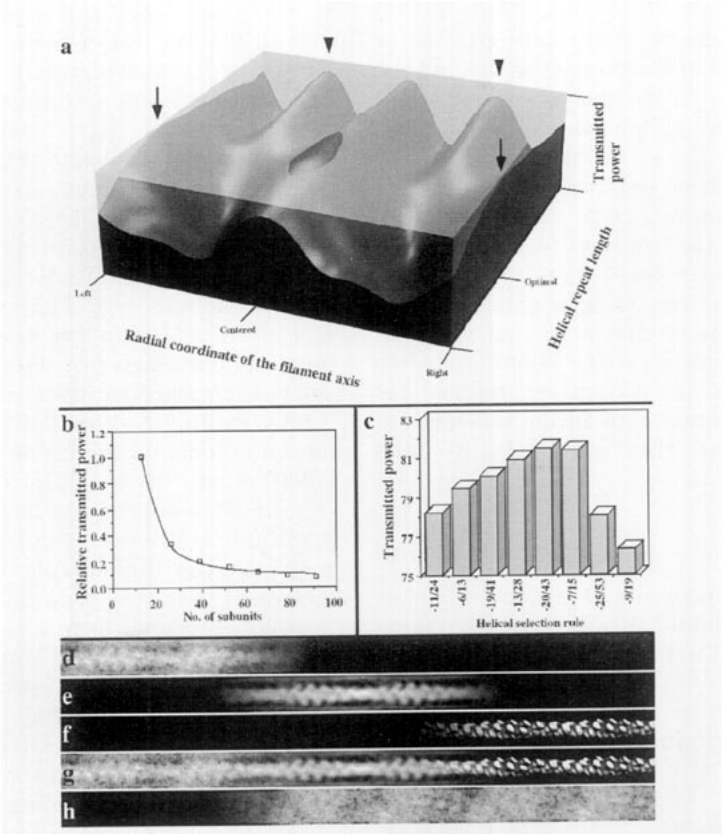

Figure 2. Image reconstruction of negatively stained F-actin filaments: quantitative analysis, determination and optimization of helical parameters. a, A 3-D plot: transmitted power upon $D(Z, k)$-filtration *versus* helical repeat length and the radial coordinate of the filament axis. b, A 2-D plot: transmitted power upon $D(Z, k)$-filtration *versus* the number of subunits that contribute to the transform. c, A 2-D plot: normalized transmitted power upon $D(Z, k)$-filtration histogrammed *versus* different helical selection rules tested. d, Digitally unbent F-actin filament. The original filament length corresponded to the length of the box. The image was multiplied by a mask with a linear ramp from 0 to 1 to produce the fading out of the filament towards the right. e, The filament in d was optimized for its helical parameters and is shown after $D(Z, k)$-filtration, again multiplied with a fade-out mask. f, The $D(Z, k)$-filtered filament shown in e was 3-D reconstructed and surface-rendered. It too is shown multiplied with a fade-out mask. g, This composite filament is the sum of d, e and f. It illustrates how 3-D information is gradually retrieved from raw filament data. h, A composite filament similar to that in g was generated. It consisted of the sum of d and the $D(Z, k)$-filtered filament in e with a fade-out ramp on the left side only. Shown is the difference between this composite filament and the raw data. The difference is the image information that was not compatible with the assumed helical symmetry.

the number of subunits n in the raw image, unbent CTEM images of more than seven-crossover long F-actin filaments have been $D(Z, k)$-filtered including increasing numbers of helical repeats. In Figure 2b, the transmitted power is plotted *versus* the number of subunits for such filament stretches. Assuming that the transmitted power was inversely proportional to $\sqrt{n}$ resulted in an excellent fit of the data (correlation coefficient $r^2 = 0{\cdot}999$). For all ten F-actin filament stretches chosen to be included in the optimized averaged 3-D reconstruction $\Sigma 10$ (see Figures 4b and 7), we have computed the same curves as shown in Figure 2b. These were then used to normalize the maxima of the transmitted power relative to a fixed number, n, of subunits. Figure 2c documents that the transmitted power is sensitive to small changes in the assumed helical selection rule $l = un + vm$ upon $D(Z, k)$-filtration. These data represent the average of ten filament stretches taken from those STEM ADF images that were eventually used to generate an averaged F-actin filament 3-D reconstruction (see Figures 4b and 7). For these ten filament stretches (see Figure 4a), the optimal average helical selection rule was $l = -20n + 43m$ ($\psi = -167{\cdot}44°$), and it yielded an average transmitted power of 81·5% upon $D(Z, k)$-filtration (Figure 2c). For comparison, the average transmitted power for the helical selection rule $l = -7n + 15m$ ($\psi = -168{\cdot}00°$) was very similar, i.e. 81·4%. In contrast, the average transmitted power for the helical selection rule $l = -6n + 13m$ ($\psi = -166{\cdot}15°$) that is generally assumed to describe the helical symmetry of the F-actin filament well (Bremer *et al.*, 1991), was only 79·5%. As can be depicted from Figure 2c, increasing the screw angle ψ by 3°, i.e. from $\psi = -167{\cdot}4°$ (corresponding to the optimal helical selection rule $l = -20n + 43m$) to $\psi = -170{\cdot}5°$ (corresponding to the helical selection rule $l = -9n + 19m$), resulted in a decrease of the average transmitted power from 81·5% to 76·3%.

The different steps used for image reconstruction as described above are summarized in Figure 2d to h: panel d shows an unbent filament stretch; panel e

displays the same filament after helix parameter optimization and $D(Z, k)$-filtration; panel f shows the same filament after 3-D reconstruction and surface-rendering. Panel g is a composite filament that illustrates how the structural information contained in the raw image becomes gradually more evident with each processing step. Panel h displays the difference between the raw data filament stretch that was used to generate panel d and a composite filament made from the raw data in panel d and a $D(Z, k)$-filtered filament stretch as in panel e that extended to the right margin of the Figure. Since no remaining information or "negative replica" is evident, a maximum amount of image information was transferred from the raw data to the reconstruction.

(b) *Selecting contouring levels for surface-rendering*

A realistic surface-rendered 3-D reconstruction of an F-actin filament should ideally have the same maximum diameter as the F-actin filament itself: i.e.

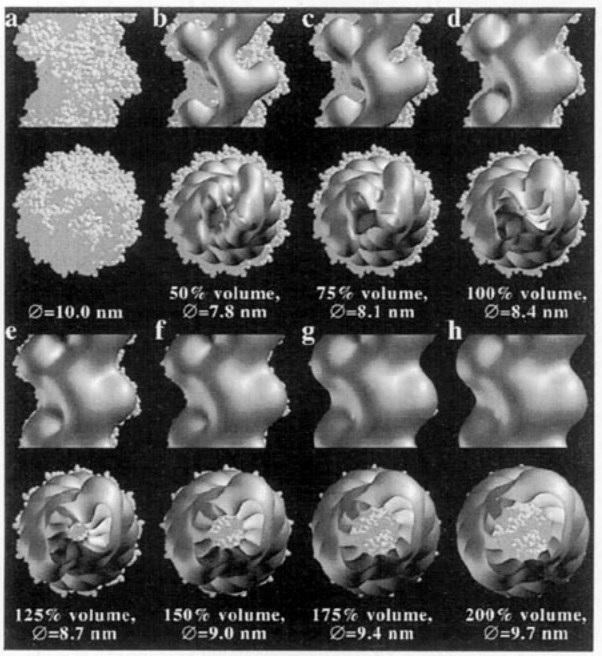

Figure 3. Calibration of the contouring levels used for solid-surface rendering of 3-D reconstructions. A CPK representation of an atomic model of the actin filament (Holmes *et al.*, 1990) was used to calibrate the contouring level for surface-rendering of an average of 10 individual F-actin filament 3-D reconstructions, termed Σ10. The CPK representation and the surface-rendered Σ10 have been computed in parallel projection, i.e. lacking perspective. a, The CPK representation has a maximum diameter of 10·0 nm when measured on an end-on view (lower panel). b to h, Σ10 has been surface-rendered in 25% increments to include between 50% (b) and 200% (h) of the nominal molecular volume. Σ10 is shown aligned with, and in front of the CPK representation. The percentage of the included nominal molecular volume (calculated assuming a hydrated protein density of 0·81 Da/Å^3) as well as its maximum diameter determined from end-on views (lower panels) are indicated below the panels.

9·0 to 9·5 nm (for reviews, see Holmes & Kabsch, 1991; Bremer & Aebi, 1992). As illustrated in Figure 3, to calibrate our contouring level for surface-rendering, we have surface-rendered a 3-D reconstruction to include different nominal molecular volumes (i.e. assuming a hydrated protein density of 0·81 Da/Å^3) and investigated its maximum end-on view diameter. The reconstruction used was Σ10, an average of ten individual F-actin filament reconstructions (see Figures 4b and 7). Including 150% of the nominal molecular volume produced a maximum diameter of 9·0 nm (see Figure 3f). This surface-rendered reconstruction smoothly envelops a Corey-Pauling-Koltun (CPK) representation of an atomic model of the actin filament (Holmes *et al.*, 1990) shown in the background. As can be seen in Figure 3b, a contouring level to include 50% of the nominal molecular volume is very suitable to represent the intersubunit contact pattern along and between the two long-pitch helical strands. To facilitate comparison, we have contoured all reconstructions shown throughout the remainder of the Figures to include either 50% or 150% of the nominal molecular volume.

A correct value for the hydrated protein density of the actin subunit should yield the correct filament diameter for a thresholding level selected to include 100% of the nominal molecular volume. However, a nominal volume of 150% was required to yield the correct filament diameter with our reconstructions. Therefore, the assumed hydrated protein density of 0·81 Da/Å^3 (Taylor & Amos, 1981) may be too high by a factor of 1·5. Independent of our volume calibration, a hydrated protein density of 0·81 Da/Å^3 yields 51·5 kDa/nm for a solid cylinder with a diameter of 9·0 nm (i.e. that of the F-actin filament). Since 13 subunits of 43 kDa each per 35·7 nm helical repeat amounts to 15·7 kDa/nm, the F-actin filament would occupy only 30·5% of the cylinder volume. This fraction of occupied volume is probably too low and a more realistic estimate of about 50% corresponds to about 25 kDa/nm. Again, this value amounts to approximately 160% of the expected 15·7 kDa/nm (see above), in line with our calibration. Accordingly, 0·50 to 0·55 Da/Å^3 may represent a more realistic estimate for the hydrated protein density of the F-actin subunit in the filament.

(c) *How much averaging is required?*

Electron micrographs recorded under low-dose conditions are generally noisy and thus require averaging to arrive at a statistically significant signal-to-noise ratio (for a review, see Bremer *et al.*, 1992). The 3-D reconstructions of ten individual F-actin filament stretches for which the helical parameters were optimized as outlined above are presented in Figure 4a. These reconstructions were computed over filament stretches including between 41 and 56 subunits each, are displayed in randomized order, and were averaged after interpolation to the helical selection rule $l = -6n + 13m$ and rotational and translational alignment. Their incremental

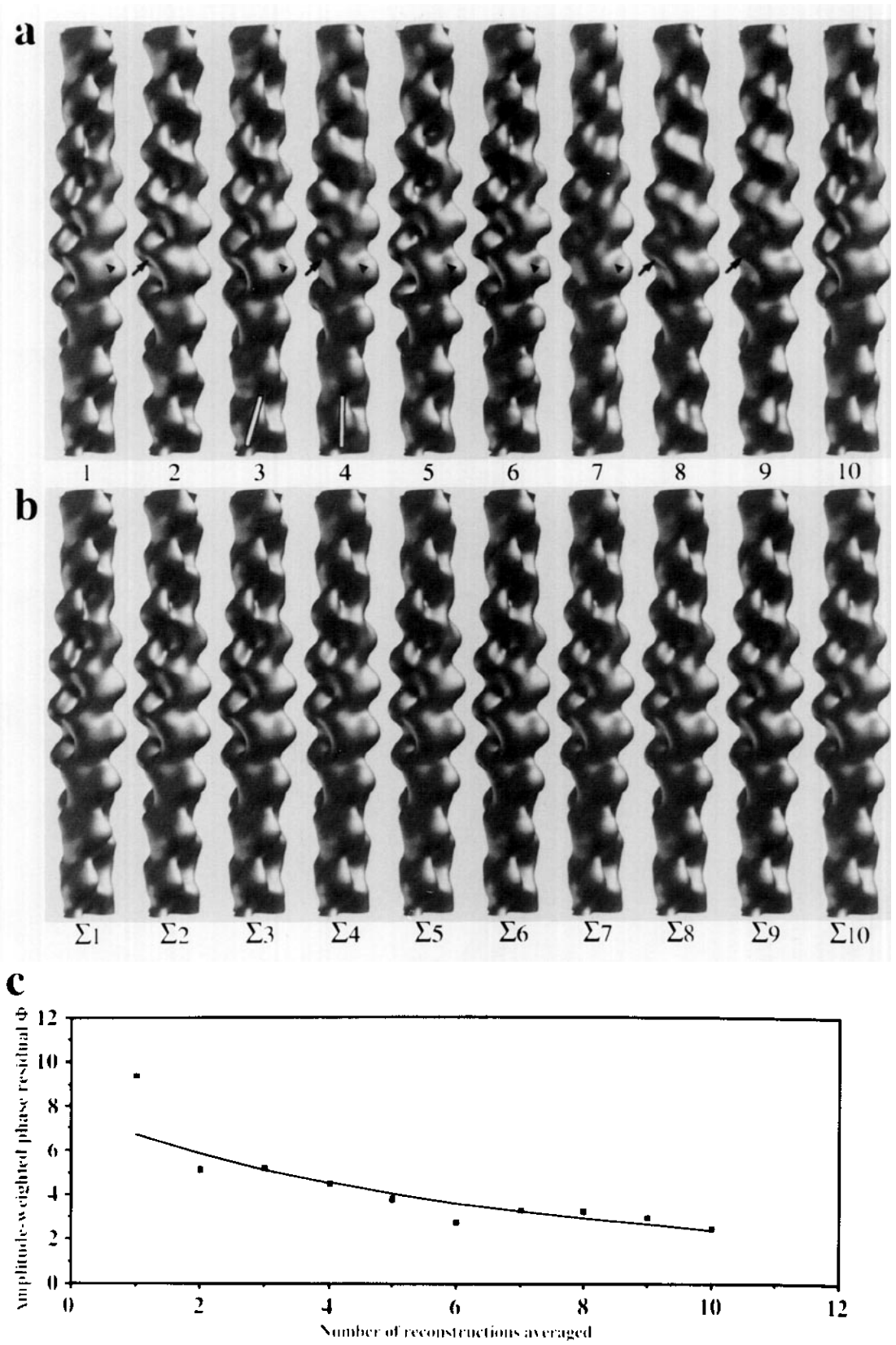

Figure 4. Individual F-actin filament 3-D reconstructions and their incremental averages. a, Ten individual F-actin filament stretches have been reconstructed using an automated 3-D helical parameter search as described in the text. The reconstructions are shown aligned and in randomized order, and they have been surface-rendered to include 150% of the nominal molecular volume (see Figure 3). The number below each reconstruction is used to refer to it in the text. The lines drawn on reconstructions 3 and 4 highlight the inclination of the long axis of the smaller outer domain of the actin subunit. Arrowheads point at the interdomain cleft in reconstructions 1 and 3 to 7. Arrows point at the connectivity between the two strands (i.e. between subdomain 4 of a subunit from one strand and the closest subdomain 1 of a subunit from the opposite strand) in reconstructions 2, 4, 8 and 9. b, From the reconstructions 1 to 10 shown in a, the corresponding incremental averages Σ1 to Σ10 have been computed (e.g. Σ3 is the average of reconstructions 1 to 3 in a). c, The amplitude-weighted phase residuals ϕ of the incremental averages Σ1 to Σ10 are shown plotted *versus* the number of reconstructions averaged. The fit shown is inversely proportional to $\sqrt{\text{number of reconstructions}}$.

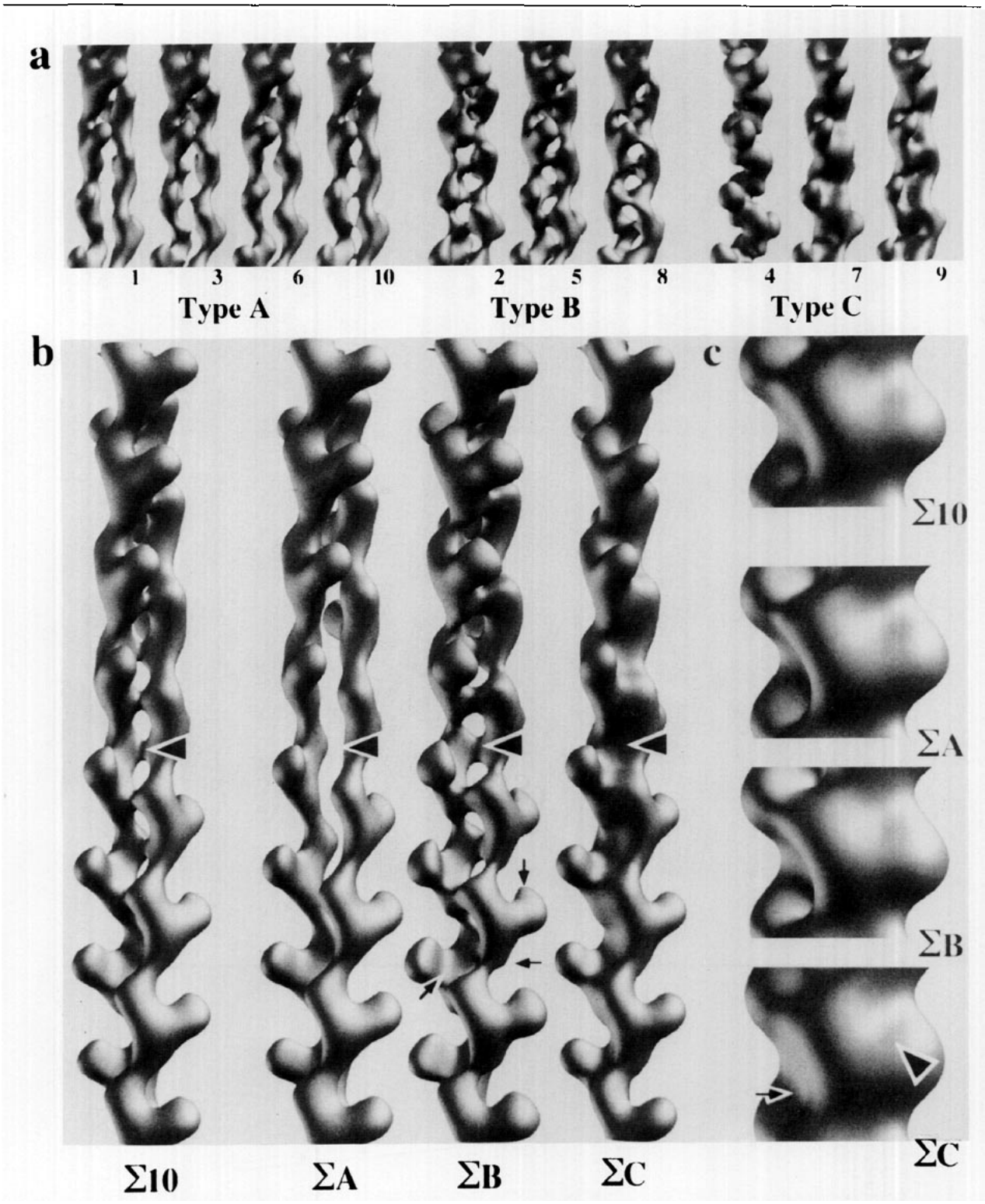

Figure 5. Distinct types of intersubunit contact patterns. a, The reconstructions 1 to 10 from Figure 4a are shown surface-rendered to include 50% of their nominal molecular volume. They are classified into 3 distinctive types of reconstructions according to their intersubunit contact pattern: type A exhibits strong long-pitch helical contact and little if any contact between the two strands; type B reveals continuous strong contact along and interrupted contact between the 2 long-pitch helical strands; finally, type C shows predominant contact between the 2 strands. b, The reconstructions of the 3 types A, B and C shown in a were averaged separately, and the resulting subaverages ΣA, ΣB, and ΣC are compared with the overall average Σ10, all surface-rendered to include 50% of the nominal molecular volume. Arrows identify areas that clearly differ among the subaverages in addition to the relative strength of the intersubunit contacts between the two long-pitch helical strands that was used to classify the reconstructions in the first place (see arrowheads). c, The subaverages ΣA, ΣB and ΣC, and the overall average Σ10 are shown surface-rendered to include 150% of the nominal molecular volume. In ΣC, the arrowhead indicates the interdomain cleft that separates the larger inner from the smaller outer domain while the arrow points at the interstrand contact interface.

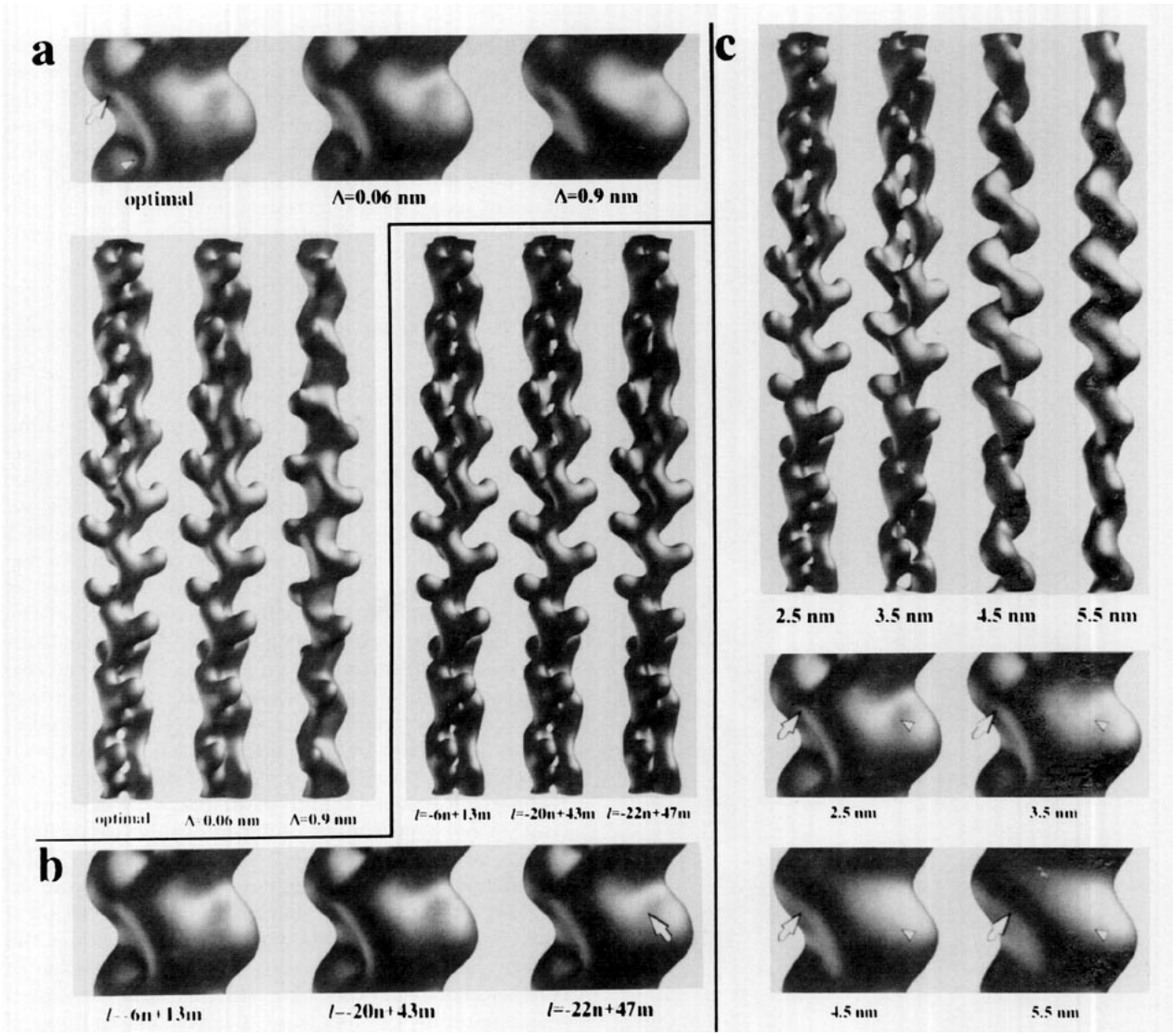

Figure 6. Phenotypes of F-actin filament reconstructions resulting from deviations from the optimal helical parameters, and from different nominal resolutions. a, Effects of deviating from the optimal radial coordinate of the filament axis on the phenotype of the F-actin filament 3-D reconstructions. The 10 F-actin filament stretches that were included in Σ10 have been reconstructed with the filament axis radially shifted as indicated, averaged and are compared to the optimal reconstruction Σ10. The helical repeat length was optimized after displacing the radial coordinate of the filament axis. All reconstructions are shown surface-rendered to include 150% (top) and 50% (bottom) of the nominal molecular volume. The arrow highlights the connectivity between subdomain 4 of one subunit from one long-pitch helical strand with subdomain 1 of the closest subunit from the other strand. The arrowhead points at a region of the interstrand interface where structural detail deteriorates when displacing the filament axis. b, Effect of the imposed helical selection rule on the phenotype of F-actin filament 3-D reconstructions. The filament stretches that were included into Σ10 have been reconstructed assuming the helical selection rules indicated. All averaged reconstructions are shown surface-rendered to include 150% (bottom) and 50% (top) of the nominal molecular volume. The arrow indicates the interdomain cleft separating the larger inner and the smaller outer domain of the actin subunit. c, Effect of lowering the nominal isotropic resolution on the phenotype of the F-actin filament 3-D reconstructions. The nominal resolution of Σ10 from Figures 4b and 7 has been reduced from 2·5 to 3·5, 4·5 or 5·5 nm by multiplying its Fourier transform with the corresponding circular Gaussian-edged mask. The resulting resolution-limited data sets were then 3-D reconstructed. The nominal resolution is indicated below each reconstruction. All reconstructions are shown surface-rendered to include 150% (bottom) and 50% (top) of the nominal molecular volume. While the arrow highlights the same feature as in a, the arrowhead points at the interdomain cleft.

averages Σ1 to Σ10 are shown in Figure 4b (e.g. Σ3 in Figure 4b is the average of reconstructions 1, 2 and 3 from Figure 4a). Comparing the incremental averages Σ1 to Σ10 at a contouring level to include 150% of the total molecular volume documents that averaging over only three or four independent F-actin filament reconstructions already yields stable averages (i.e. averaging more reconstructions does not result in significant structural changes anymore). Very similar results were obtained with other randomized filament orders. For a more quantitative evaluation of the incremental averages, we have computed their amplitude-weighted phase residual Φ:

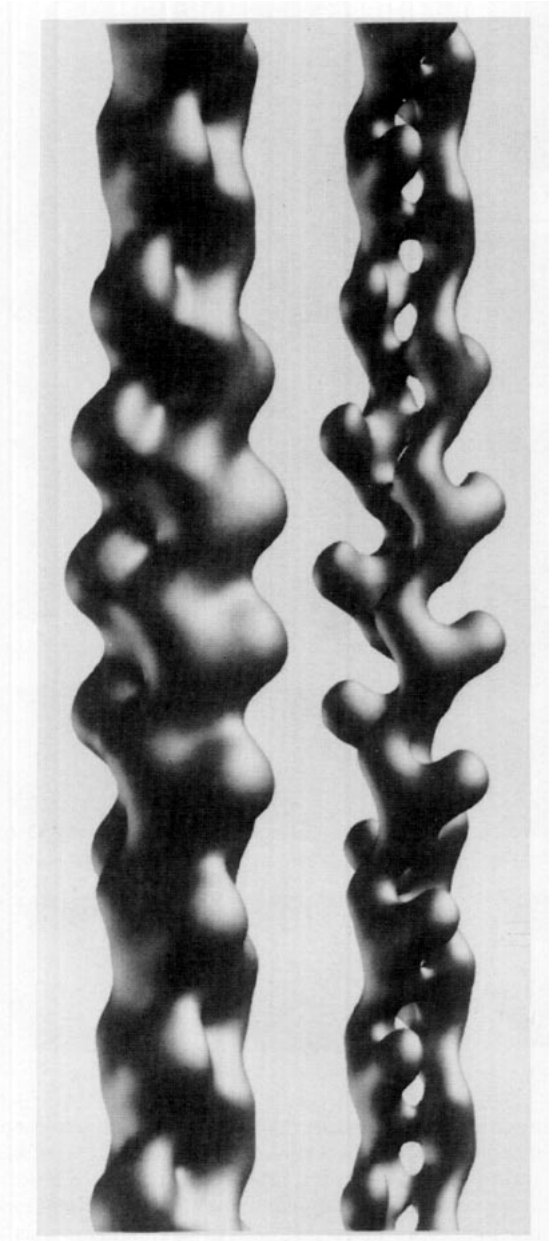

Figure 7. Structure of Σ10, an average of 10 F-actin filaments polymerized with 2 mM $MgCl_2$ and 50 mM KCl. See Figure 4a for the individual reconstructions contained in the average. Σ10 is shown to the left surface-rendered to include 150% of the nominal molecular volume and to the right to include 50% of the molecular volume.

$$\Phi = \frac{\sum_r |F| \cdot |\phi_l - \phi_r - n\pi - 2k\pi|}{\sum_r |F|},$$

where F is the averaged amplitude at reciprocal radius r; ϕ_l and ϕ_r are phases of the left and right halves of the transform at reciprocal radius r; n is the Bessel order predicted by the helical selection rule; k is an integer so that $-\pi \leqslant \phi_l - \phi_r \leqslant \pi$.

As documented in Figure 4c, Φ computed along the layer-lines of the incremental averages out to reciprocal radii of $(2{\cdot}5\ \text{nm})^{-1}$ drops from initially 10 to 12° (for individual reconstructions) to a stable value of about 3 to 4° after averaging about six or seven reconstructions. This number is in line with the number of reconstructions that is required to obtain stable averages at the 50% volume level (not shown). For raw data with an optimized radial position of the filament axis and an optimized helical repeat length but before $D(Z, k)$-filtration, Φ ranged between 20° and 25°.

(d) *Distinct types of intersubunit contact patterns.*

The overall size and shape of the different F-actin filament reconstructions was conserved, but the relative strength of the intersubunit contact along and between the two long-pitch helical strands appeared variable. We have found at least three distinct types of reconstructions. In Figure 5a we have classified the F-actin filament reconstructions 1 to 10 of Figure 4a into three types according to the relative strength of their intersubunit contacts as revealed by contouring them to include 50% of the total molecular volume: type A (i.e. reconstructions 1, 3, 6 and 10) exhibits strong contact along the two long-pitch helical strands and little if any contact between them; type B (i.e. reconstructions 2, 5 and 8) reveals significant but discontinuous contact between the two long-pitch helical strands; and type C (i.e. reconstructions 4, 7 and 9) displays predominant contact between the two long-pitch helical strands. Only two of the ten reconstructions differ significantly from the others: reconstruction 4 and, to a lesser extent, reconstruction 2. Reconstruction 4 has predominant intersubunit contact along the genetic helix. We scored this as an extreme case of contact between the two strands and classified reconstruction 4 as type C. Reconstruction 2 (classified as type B; Figure 5a) is unusual in that the shape of its subunit also appears to be quite massive. It is noteworthy that these two reconstructions look quite inconspicuous at the 150% volume level (see Figure 4a), demonstrating that reconstructions should not just be judged by looking at one contouring level. Omitting reconstructions 2 and 4 from Σ10 did not result in significant structural changes of the remaining average Σ8 (not shown). Out of the ten reconstructions shown in Figure 4a and 5a, the number of F-actin filament reconstructions that fell into the groups A, B and C was similar: four of type A and three each of type B and type C. Other independent sets of reconstructions that were not included in Σ10 yielded similar distributions into the three types A, B and C (data not shown).

For the three distinct F-actin filament 3-D reconstruction types A, B and C, we have computed the corresponding subaverages ΣA, ΣB and ΣC, and these are shown in Figure 5b and c, together with the overall average Σ10. In Figure 5b, the arrowheads highlight where the differences in the relative strength of the intersubunit contacts along and between the two long-pitch helical strands are most distinct at the 50% volume contouring level. In addition, the shapes of the high-mass density regions of the subunit also

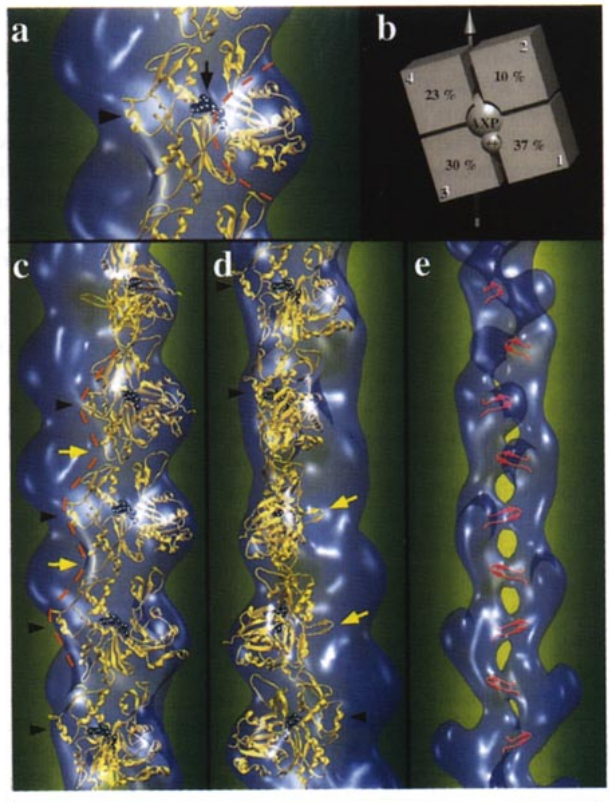

Figure 8. Comparison of the averaged F-actin filament 3-D reconstruction Σ10 with the atomic structure of the actin filament: towards atomic interpretation of F-actin filament 3-D reconstructions. a, A short stretch of the 3-D reconstruction Σ10 (see Figures 4b and 7) is displayed contoured to include 150% of the nominal molecular volume. The reconstruction was aligned with and is shown transparently overlaid onto a ribbon representation of one long-pitch helical strand of an atomic model of the actin filament (Holmes *et al.*, 1990). The interdomain cleft (highlighted by a broken line) separates subdomain 1 from subdomains 2, 3 and 4. It runs at an angle of approximately 45° tracing the region of lowest density between subdomains 1 and 2. As the cleft reaches the nucleotide binding site (see arrow), it changes its direction by about 90° to follow the region of lowest density between subdomains 1 and 3. The arrowhead points at the α-helix 222-233. b, A schematic perspective view of the subdomain structure of the actin subunit (adapted from Bremer & Aebi, 1992). The position of the specifically bound nucleotide (AXP) as well as its associated divalent cation (+ +), and the numberings of the subdomains together with their relative molecular masses (according to Kabsch *et al.*, 1990) are indicated. The approximate position of the filament axis is depicted by the arrow with the arrowhead pointing to the pointed end of the F-actin filament with respect to the myosin S-1 decoration pattern. a and b are approximately aligned and to scale. For the sake of clarity, the model in b is tilted relative to the reconstruction shown in a by 10° horizontally and vertically. c and d, Comparison of Σ10 with an atomic model of the actin filament. Σ10 was contoured to include 150% of the nominal molecular volume and is shown aligned with and transparently overlaid onto a ribbon representation of one long-pitch helical strand of an atomic model of the actin filament (Holmes *et al.*, 1990). The subunits are slightly tilted with respect to the filament axis (see a and b), resulting in a zigzagging line that defines the outer margin of a long-pitch helical strand in the interface between the 2 strands (see dotted line). One of the turns of this zigzagging line is defined by the α-helix 222-233 (arrowhead) that extends from the rest of subdomain 4 like a handle (see also arrowhead in a). The other bend of the zigzagging line can be explained as the contact interface of subunits that are adjacent along one long-pitch helical strand (see arrows). c and d are rotated relative to each other by 110°. e, Testing a prediction of the atomic model of the actin filament. Σ10 has been contoured to include 50% of the nominal molecular volume. The atomic model (Holmes *et al.*, 1990) has been aligned with Σ10 and ribbon representations of the hydrophobic loops only have been computed and are shown overlaid: they extend through the rung-like intersubunit connectivity across the 2 long-pitch helical strands, the bridges in our terminology. The filaments in d and e are oriented identically.

appear to be variable to some extent, particularly around the smaller outer domain of the actin subunit (see arrows in ΣB). ΣB reveals distinct additional structural features (see arrows) that are absent from ΣA, ΣC and Σ10. When contoured to include 150% of the total molecular volume as in Figure 5c, ΣA and ΣB are quite similar to each other as well as to the overall average Σ10. ΣC appears filled and less structured in the interstrand contact region (see arrow). Furthermore, as pointed to by the arrowhead in Figure 5c, the separation between the larger inner and the smaller outer domain through the interdomain cleft is less obvious in ΣC than it is in ΣA, ΣB or Σ10.

(e) *Phenotypes of F-actin filament reconstructions that arise from suboptimal processing or from lowering the resolution*

We have systematically investigated the phenotypes of reconstructions that are observed when

deviating from the optimal helical parameters as determined in our 3-D helical parameter search. In agreement with the relatively shallow gradient in the transmitted power upon $D(Z, k)$-filtration that is observed when changing the helical repeat length (see Figure 2a), deviating from the optimal helical repeat length produces only minor effects on the structure of F-actin filament 3-D reconstructions, and these are therefore not shown. In contrast, the same 3-D reconstructions are sensitive to even small deviations from the optimal radial position of the filament axis. As illustrated in the top panel of Figure 6a, deviating from the optimal radial position of the filament axis by as little as 1 nm yields a rather pronounced mass redistribution from several parts of the surface of the subunit into the connectivity between the two long-pitch helical strands (see the region marked by the arrow). As a result, the concavity between the two strands becomes filled (see the region indicated by the arrowhead). Hence the detailed morphology of the contact pattern between the two long-pitch helical strands is extremely sensitive to deviations from the optimal radial coordinate of the filament axis. As documented in Figure 7 (right), the optimal averaged F-actin filament 3-D reconstruction $\Sigma 10$ reveals continuous contact along and discontinuous contact between the two long-pitch helical stands. The lower panel of Figure 6a illustrates that shifting the radial coordinate of the filament axis causes a gradual transition from a ladder-like to an uninterrupted intersubunit contact pattern between the two long-pitch helical strands. It is remarkable that a shift of the radial coordinate by as little as 0·06 nm already produces significant effects.

Averages of the same ten filament stretches have also been computed assuming different helical selection rules. As illustrated in Figure 6b (top and bottom panels), 3-D reconstructions computed assuming $l = -6n + 13m$ ($\psi = -166{\cdot}15°$) and $l = -20n + 43m$ ($\psi = -167{\cdot}44°$) appear similar to each other. Assuming $l = -22n + 47m$ ($\psi = -168{\cdot}51°$), however, affects the morphology of the intersubunit contact between the two long-pitch helical strands significantly (see the upper panel of Figure 6b). It is interesting to note that in the case of the suboptimal helical selection rule $l = -22n + 47m$ ($\psi = -168{\cdot}51°$) its screw angle differs by $+1{\cdot}07°$ from that of the optimal helical selection rule $l = -20n + 43m$ ($\psi = -167{\cdot}44°$), whereas in the case of $l = -6n + 13m$ ($\psi = -166{\cdot}15°$), the helical selection rule generally assumed to describe the helical symmetry of the F-actin filament well (see Bremer *et al.*, 1991), it differs by $-1{\cdot}29°$. Hence it appears that primarily the sign and not the magnitude of the deviation from the optimal screw angle determines the degree of deterioration of structural detail upon enforcing a particular helical selection rule *via* $D(Z, k)$-filtration. This behavior correlates nicely with the transmitted power upon $D(Z, k)$-filtration (see Figure 2c). As can be further depicted from Figure 6b, assuming the suboptimal helical selection rule $l = -22n + 47m$ deteriorates the intersubunit contact pattern between the two long-pitch helical strands, and degrades some of the structural detail of the actin subunit. At the 150% volume contouring level, the structural differences among the three different helical selection rules shown become more subtle than at the 50% volume contouring level (compare top with bottom panel in Figure 6b). Accordingly, the 3-D reconstructions computed with the helical selection rules $l = -6n + 13m$ and $l = -20n + 43m$ reveal minimally more mass at the tip of the smaller outer domain than that computed with $l = -22n + 47m$. However, the interdomain cleft becomes clearly less pronounced with the latter reconstruction (see arrow) compared with the other two reconstructions.

We have shown previously that electron density maps of the atomic model of the F-actin filament reveal a dramatic transition in their intersubunit contact pattern when reducing the nominal resolution isotropically (Bremer *et al.*, 1992): at nominal isotropic resolutions $\leqslant 3{\cdot}0$ nm the contact along the two long-pitch helical strands is significantly stronger than between them (see Figure 12 by Bremer *et al.*, 1992). At nominal isotropic resolutions >3·0 nm, the situation becomes reversed. As shown in the top panel of Figure 6c, similar transitions are observed when the resolution of $\Sigma 10$ was isotropically reduced to less than 3·5 nm. Likewise, reducing the radial resolution only also blurs the details of the intersubunit contact interface between the two strands, primarily the ladder-like contact between the two long-pitch helical strands (data not shown). By contrast, reducing the resolution axially only has little effect on the 3-D structure of the filament within the range of nominal resolutions tested (data not shown). At the 150% volume contouring level, a more massive, less structured connectivity between the two strands builds up when reducing the nominal resolution of the reconstruction isotropically from 2·5 to 3·5 nm (see arrows in the bottom panel of Figure 6c). Reducing the resolution further to 4·5 or 5·5 nm eventually fills the concavity in the intersubunit contact interface between the two strands. The interdomain cleft separating the larger inner from the smaller outer domain of the actin subunit is visible only when the isotropic nominal resolution is 3·5 nm or better (see arrowheads in the bottom panel of Figure 6c).

(f) *The variability of 3-D reconstructions*

At first glance, the overall morphology of the ten reconstructions displayed in Figure 4a appears remarkably similar; however, closer inspection reveals subtle differences among them. To evaluate these differences in a more systematic way, we have aligned our optimized averaged F-actin filament 3-D reconstruction $\Sigma 10$ (see Figure 7) with the atomic model built by Holmes *et al.* (1990). In Figure 8a, an overlay of part of the $\Sigma 10$ reconstruction with a ribbon representation of one long-pitch helical strand of the atomic model is shown. Comparison with a schematic view of the actin subunit (Figure 8b; adapted from Bremer & Aebi, 1992) reveals that

subdomains 1 and 3 of the actin molecule account for the massive base (i.e. 67% of the subunit mass) of the subunit while its more slender tip consists of subdomains 2 and 4 (i.e. 33% of the subunit mass). Subdomains 3 and 4 are located at relatively low filament radii and constitute the larger inner domain, whereas subdomains 1 and 2 are located at higher filament radii and comprise the smaller outer domain.

Comparing the individual reconstructions in Figure 4a reveals that the orientation of the smaller outer domain relative to the filament axis varies among reconstructions. This is highlighted in reconstructions 3 and 4 of Figure 4a by a line drawn to define the long axis of the smaller outer domain. Accordingly, in reconstructions 3, 7 and 9 this axis is tilted by roughly 15 to 20° relative to the filament axis (this is best seen with the first subunit of the left strand at the bottom of the reconstructions), whereas in reconstructions 2, 4 and 10 this axis is almost parallel with the filament axis. The individual reconstructions also vary in the morphology of their interstrand interface, i.e. in the region where the two long-pitch helical strands establish contact. A dominant feature in reconstructions 2, 4, 8 and 9 of Figure 4a is the distinct connectivity between subdomain 4 of one subunit of one long-pitch helical strand with subdomain 1 of the nearest subunit of the opposite strand (see arrows). The interdomain cleft separating the two domains of the molecule is best seen at the level of the fourth subunit from the bottom along the left long-pitch helical strand: it appears quite variable, ranging from barely visible (reconstructions 2; and 8 to 10) to relatively prominent (see arrowheads in reconstructions 1, and 3 to 7).

(g) *Interpretation of F-actin filament 3-D reconstructions at the level of distinct secondary structure elements*

As illustrated in Figure 3, the optimized averaged filament Σ10 appears like a low-pass filtered representation of the atomic model of the actin filament (Holmes *et al.*, 1990). A pronounced interdomain cleft (indicated by a red broken line in Figure 8a) separates the larger inner from the smaller outer domain in the Σ10 reconstruction. This interdomain cleft first runs at an angle of 40 to 45° relative to the filament axis along the interface (i.e. following the lowest density) between subdomains 1 and 2, until it reaches the region of the nucleotide and divalent cation binding site (arrow) where it changes its orientation by almost 90° to follow the interface between subdomains 1 and 3.

As displayed in Figure 8a and b, to a first approximation the actin subunits are rectangular and slightly tilted with respect to the filament axis. Therefore, the outer edges of subdomains 3 and 4 of the subunits along each of the two long-pitch helical strands define a zigzagging line (see the red broken line in Figure 8c). The handle-like α-helix 222–233 (see the black arrowheads in Figure 8c and d; see also Figure 8a and Kabsch *et al.*, 1990) is a very distinctive structural feature of the actin molecule (see Figure 1 of Bremer & Aebi, 1992) and it molds the convex part of this zigzagging line. The intersubunit contact interface between subunits that are adjacent along the long-pitch helical strands defines the concave part of the zigzagging line (see the yellow arrows in Figure 8c).

In the orientation shown in Figure 8d, an unmistakable feature of the atomic model is the "hydrophobic loop" (i.e. residues 262 to 274; Kabsch *et al.*, 1990) that extends from each subunit towards and across the filament axis (see the yellow arrows). The right panel of Figure 7 illustrates that rung-like intersubunit contacts with one connecting "bridge" per subunit hold the two long-pitch helical strands of Σ10 together. Both the hydrophobic loop and this bridge of high mass density originate from the region close to the interface between subdomains 3 and 4 (see the yellow arrows in Figure 8d). In Figure 8e, we have overlaid the optimized averaged Σ10 filament 3-D reconstruction surface-rendered to include 50% of the nominal volume with a ribbon representation of only the hydrophobic loops of the atomic model of the actin filament (Holmes *et al.*, 1990). These loops coincide with the high-density bridges that connect the two long-pitch helical strands of Σ10.

4. Discussion

We have produced molecular resolution reconstructions of F-actin filaments polymerized *from Ca-ATP-G-actin with 2 mM* $MgCl_2$ *and 50 mM* KCl which, by comparison with an atomic model (Holmes *et al.*, 1990), can be interpreted at the level of distinct secondary structure elements. This was achieved by optimizing the helical processing strategy for 3-D reconstruction of STEM ADF images of negatively stained F-actin filaments.

(a) *Towards atomic interpretation of F-actin filament 3-D reconstructions*

A number of proteins and/or their supramolecular assemblies have been investigated both by EM at the molecular level (typically in the range of 1·0 to 3·5 nm resolution), and by X-ray crystallography at atomic detail. Examples include actin (reviewed by Reisler, 1993), myosin S-1 (Rayment *et al.*, 1993*a*, *b*; Schröder *et al.*, 1993), bacterial porin (Cowan *et al.*, 1992; Engel *et al.*, 1992), and several viruses (e.g. TMV; Unwin & Klug, 1974; Jeng *et al.*, 1989; Namba & Stubbs, 1986).

Comparing our optimized F-actin filament 3-D reconstruction Σ10 with an atomic model of the actin filament (Holmes *et al.*, 1990) demonstrates that molecular resolution EM data can be used to critically evaluate specific predictions made by atomic models. As illustrated in Figure 3, Σ10 very closely envelops a CPK representation of the Holmes model (Holmes *et al.*, 1990), and Figure 8 documents that this structural agreement between Σ10 and the atomic model extends beyond the molecular surface. Holmes and co-workers remodeled the hydrophobic loop (residues 262 to 274) from the kinked conformation found in the crystal structure of actin (Kabsch *et al.*,

1990) to an extended β-hairpin and predicted its plug-like insertion into a hydrophobic pocket formed by the interface between two adjacent subunits of the opposite long-pitch helical strand (Holmes *et al.*, 1990). Overlaying Σ10 with the atomic model reveals that the hydrophobic loop in fact coincides with the distinct high-mass density bridge that connects the two long-pitch helical strands every 2·75 nm in our reconstruction. This is the first direct structural confirmation of a prediction of an atomic model that lacked any experimental evidence. Recently, the hydrophobic loop hypothesis was tested by Rubenstein and co-workers (Chen *et al.*, 1993), who used site-directed mutagenesis to introduce a hydrophilic residue into the hydrophobic loop of yeast actin by substituting Asp for Leu266. This point-mutated actin barely polymerized at low temperature, and its cold-sensitive phenotype was interpreted as indicating poor nucleation of polymerization (for a review, see Pollard, 1990) due to a conformation of the hydrophobic loop that is different from the wild-type actin homolog. Together with these mutation experiments, our structural data provide strong evidence in favor of the hydrophobic loop being an extended β-hairpin in the F-actin conformation as proposed by Holmes and co-workers (Holmes *et al.*, 1990; Lorenz *et al.*, 1993).

Inserting the hydrophobic loops of one long-pitch helical strand into the complementary hydrophobic pockets provided by the other strand suggests a molecular "zipper". A model to explain the intrinsic F-actin filament disorder, the lateral slipping model, that is very compatible with such a molecular zipper was proposed a few years ago (Aebi *et al.*, 1986; Bremer *et al.*, 1991). The lateral slipping model assumes that short stretches of subunits (i.e. $\leqslant 6$) along either one of the two long-pitch helical strands may deviate collectively from their position in an ideal helix. This lateral slipping produces filaments with variable maximal width and variable crossover spacing. More recently, a "rotational stagger" formalism describing the angular component of lateral slipping was proposed (Censullo & Cheung, 1993). It allows a quantitative explanation of the variable crossover spacings measured along individual F-actin filaments as they were shown by Bremer *et al.* (1991).

Extending our investigation to interpret F-actin filament 3-D reconstructions at the secondary structure level, we have computed 3-D reconstructions of F-actin filaments polymerized from Ca-ATP-G-actin with 100 mM KCl in the absence and presence of stoichiometric amounts of the mushroom toxin phalloidin (unpublished results). The same polymerization conditions were employed to produce the X-ray fiber diffraction patterns used to calculate refined atomic filament models (Lorenz *et al.*, 1993). We are currently scrutinizing the structural agreement between these two refined atomic filament models and the corresponding EM-based 3-D reconstructions.

EM and X-ray data can synergistically complement each other when investigating functional states that are not directly amenable to structural analysis at the atomic level. For example, the structure of ATP-F-actin filaments cannot be elucidated easily by X-ray fiber diffraction since the temporal resolution of this method (see Popp *et al.*, 1987) is much lower than the half-life of ATP-F-actin filaments (i.e. hours *versus* seconds to minutes). Once faithful EM-based 3-D reconstructions of ATP-F-actin filaments at 2 to 3 nm resolution become available, fitting atomic models into these reconstructions may nevertheless allow for an interpretation of possible conformational differences between ADP-F-actin and ATP-F-actin filaments. Atomic interpretation of EM data will probably also gain momentum to formulate atomic models for the myosin ATPase cycle. First steps towards this goal were attempts by Rayment *et al.* (1993*b*) and Schröder *et al.* (1993) to fit EM-based 3-D reconstructions of S-1-decorated F-actin filaments with an atomic model of the actin filament (Holmes *et al.*, 1990; Lorenz *et al.*, 1993) to which the atomic structure of the myosin S-1 fragment (Rayment *et al.*, 1993*a*) was docked.

(b) *The helical parameter search*

As shown in Figure 2a, an absolute maximum (highlighted by the $x - y$ plane that intersects the 3-D plot surface) was always observed when plotting the transmitted power upon $D(Z, k)$-filtration *versus* the helical repeat length and the radial coordinate of the filament axis. Smaller local maxima of the power transmitted upon $D(Z, k)$-filtration (see the arrows and arrowheads in Figure 2a) were also observed.

X-ray fiber diffraction data of F-actin filaments could best be indexed by the integer helical selection rule $l = -6n + 13m$ (e.g. see Holmes *et al.*, 1990). As documented in Figure 2c, the ten filament stretches used to produce the optimized reconstruction Σ10 were best approximated by the two helical selection rules $l = -22n + 43m$ and $l = -7n + 15m$. We do not doubt that the overall helical symmetry of the F-actin filament is satisfactorily described by $l = -6n + 13m$. Nevertheless, optimizing the helical selection rule for a particular filament stretch assures maximum transmission of power from the raw data to the $D(Z, k)$-filtered image. Structural features such as the interdomain cleft separating the larger inner from the smaller outer domain (see the arrow in Figure 6b) are sensitive to this kind of optimization.

(c) *A few words about averaging and contouring*

Judged by visual inspection of our incremental averages (see Figure 4b) and their amplitude-weighted phase residuals (see Figure 4c), averaging 250 to 300 subunits (i.e. six F-actin filament reconstructions including about 41 to 56 subunits each) already produces stable averages of negatively stained filaments. Images of frozen-hydrated F-actin filament preparations may require more extensive averaging because of their lower signal-to-noise ratio. Accordingly, the F-actin filament reconstruction presented by Milligan *et al.* (1990) represents an average over

roughly 1500 subunits. Nevertheless, the most recent 3-D reconstructions of frozen-hydrated F-actin filaments (Lepault *et al.*, 1994) included numbers of subunits similar to those we have used with our negatively stained filaments, i.e. 205 to 325 subunits.

We have analyzed four filament stretches recorded in a CTEM that were suitable for image reconstruction over $\geqslant 10$ crossovers each. Assuming $l = -6n + 13m$ and including always the same number of subunits (i.e. $4 \times 10 \times 13$ subunits = 520 subunits), we computed averages from four reconstructions over ten crossovers each, from eight reconstructions over five crossovers each, from 20 reconstructions over two crossovers each, and from 40 reconstructions over one crossover each. Judged by the transmitted power and the preservation of reproducible structural detail, the two best averages were those including eight reconstructions over five crossovers each and 20 reconstructions over two crossovers each (data not shown). Accordingly, a compromise has to be made between choosing filament stretches as short as possible to minimize the amount of the intrinsic filament disorder transferred into the individual reconstructions, and yet having them long enough that the signal-to-noise ratio of the individual reconstructions is sufficient to reveal reproducible structural detail and to allow for accurate rotational and translational alignment. This is the rationale why we reconstructed filament stretches that, depending on the helical selection rule chosen, included 41 to 56 subunits (see Results).

Our calibration of the contouring levels such as shown in Figure 3 has revealed that $\Sigma 10$ has to be contoured to include 150% of the nominal molecular volume to yield the correct filament diameter. This percentage is based on assuming a hydrated protein density of 0·81 Da/Å^3 (e.g. see Taylor & Amos, 1981). As detailed in Results, only assuming a significantly lower protein density of approximately 0·5 to 0·55 Da/Å^3 for the F-actin subunit can simultaneously yield the correct filament diameter and the correct molecular volume.

(d) *F-Actin filament dynamics and the variability among 3-D reconstructions*

Comparison of the individual reconstructions 1 to 10 that we have computed reveals the following variable structural features: (1) different shapes of the subunit (see Figure 4a); (2) different relative strength of the intersubunit contacts along and between the two long-pitch helical strands (see Figure 5a and b); (3) a more or less pronounced separation of the subunit into a larger inner and a smaller outer domain by a distinct interdomain cleft (see the arrowheads in Figure 4a); and (4) different inclinations of the long axis of the F-actin subunit's smaller outer domain relative to the filament axis (see lines in reconstructions 3 and 4 of Figure 4a). Some of these variable features (e.g. (1), (3) and (4)) may result from an intrinsic flexibility of subdomain 2 as postulated by Bremer & Aebi (1992). Consistent with this notion, McLaughlin *et al.* (1993) were missing part of subdomain 2, the so-called DNase I-binding loop (i.e. residues 41 to 50), in their electron density map of the actin molecule in complex with gelsolin segment 1, and a recent model for the structure of the thin filament based on low-angle X-ray diffraction data (Squire *et al.*, 1993) suggested changes in subdomain 2 of the actin molecule relative to the conformation in the crystal structure (Kabsch *et al.*, 1990). Further support comes from the refinement of atomic models of the actin filament where Lorenz *et al.* (1993) observed that the orientation of subdomain 2 of the actin subunit (see Figure 8b) is distinctly altered upon stoichiometric binding of the mushroom toxin phalloidin to the filament. If the larger inner domain of the actin subunit forms the backbone of the filament and is relatively fixed in the filament (Erickson, 1989), a molecular "hinge" between the larger inner and the smaller outer domain, as proposed by Tirion & ben-Avraham (1993), may cause the observed variations.

It is now agreed that the F-actin filament is a dynamic structure, and that the type and amount of intrinsic flexibility and disorder of the filament are modulated by (1) the state of hydrolysis of the bound nucleotide (e.g. Janmey *et al.*, 1990; Lepault *et al.*, 1991, 1994; Bremer & Aebi, 1992; Orlova & Egelman, 1992), or (2) upon binding of small effector molecules such as phalloidin to the filament (Bremer *et al.*, 1991; Lorenz *et al.*, 1993). However, the structural analysis of presumed distinct chemical, mechanical or conformational states of the filament at the molecular level is ambiguous and very difficult: if two different states are analyzed, one well ordered (i.e. yielding high-resolution detail) and the second relatively disordered (i.e. yielding lower resolution), the corresponding 3-D reconstructions will differ structurally simply because of the different effective resolutions (see Figure 6c), and not because of an inherent structural difference. Statistical tests have been used to lend confidence in such differences (e.g. Orlova & Egelman, 1992, 1993), but clearly, these tests cannot assess any biological significance. An additional aspect arises from the variability of individual reconstructions. We distinguished three classes of reconstructions on the basis of their intersubunit contact pattern and, as is documented in Figure 5b and c, the corresponding subaverages differed significantly, and systematically, from the overall average $\Sigma 10$. In other words, any preferential inclusion or exclusion of certain types of reconstructions ("good", "bad", etc.) may introduce a strong bias into an average. In fact, 3-D reconstructions of F-actin filaments formed under different polymerization conditions (Orlova & Egelman, 1992, 1993; Lepault *et al.*, 1994) differed from each other in very much the same details (e.g. structure of subdomain 2) that were variable between our individual 3-D reconstructions (see Figure 4a and b) of filaments polymerized under identical conditions. Unfortunately, Orlova & Egelman (1992, 1993) did not report by which criteria the reconstructions they averaged were selected. Our criterion was quantitative, i.e. we

included only those reconstructions in the average that transferred most information from the raw image to the $D(Z, k)$-filtered image.

Taken together, differences observed among different reconstructions must be evaluated with caution. They may reflect, e.g. structural dynamics, different effective resolutions or different conformational states. However, the reconstructions that we have computed for filaments formed under conditions that have been used by others (Orlova & Egelman, 1992, 1993) have so far largely failed to reveal the sort of systematic structural differences that these authors have reported (unpublished results).

(e) *Comparison with previous reconstructions*

As is documented in Figure 5 and 7, the stronger of the two types of intersubunit contact in Σ10 is made along rather than between the two long-pitch helical strands (see also Bremer & Aebi, 1992; Holmes & Kabsch, 1991). This relative strength of the intersubunit contacts is in agreement with the atomic model of the actin filament (Holmes *et al.*, 1990) as refined by Lorenz *et al.* (1993) and was also previously inferred from an analysis of thermodynamic parameters of the F-actin filament (Erickson, 1989). A similar relative strength of these two types of intersubunit contact was already revealed in the first F-actin filament 3-D reconstruction by Moore *et al.* (1970), and it was observed in more recent reconstructions of negatively stained (Aebi *et al.*, 1986; Bremer *et al.*, 1991) and frozen-hydrated (Milligan *et al.*, 1990) F-actin filaments. By contrast, all the suboptimal and low-resolution phenotypes that we computed (see Figure 6) revealed the inverse situation with an increased strength of the intersubunit contact between the two long-pitch helical strands compared with Σ10. The 3-D reconstructions with this type of intersubunit contact pattern are therefore suspicious and should be interpreted with care. As demonstrated in Figure 6c, lowering the nominal resolution isotropically can transform Σ10 into almost exactly the phenotypes of reconstructions that were obtained by Trinick *et al.* (1986) and Lepault *et al.* (1994) with frozen-hydrated F-actin filaments. It is therefore conceivable that the defocus of their images has limited their isotropic resolution to less than 3·5 nm, thus explaining the intersubunit contact pattern they observed as a consequence of low resolution.

The stoichiometric interaction of actin with actin-binding proteins may also affect the conformation of the subunits and/or the relative strength of the intersubunit contacts. The 3-D reconstructions of myosin S-1 decorated F-actin filaments (Milligan & Flicker, 1987; Milligan *et al.*, 1990) and of caldesmon-containing thin filaments (Vibert *et al.*, 1993) did not unveil any significant structural differences relative to F-actin filaments. By contrast, Owen & DeRosier (1993) as well as Schmid *et al.* (1994) reported that the conformation of the actin subunit in their reconstructions of actin-scruin filaments differed from that in the Holmes model (Holmes *et al.*, 1990) as refined by Lorenz *et al.* (1993). However, a consensus on the conformational differences has yet to be established: in the reconstruction presented by Owen & DeRosier (1993), subdomain 2 appears to be rotated so as to weaken the contact along the two long-pitch helical strands, whereas in the reconstruction presented by Schmid *et al.* (1994) subdomains 1, 2 and 3 match extremely well with the atomic model but subdomain 4 is poorly defined. This is particularly surprising since the nominal resolutions of the two reconstructions are virtually identical. Some of these differences may stem from the different preparation techniques used: negative staining by Owen & DeRosier (1993) *versus* frozen-hydrated by Schmid *et al.* (1994).

F-Actin filament 3-D reconstructions can be computed to yield anisotropic, i.e. different axial and radial resolution. Accordingly, reducing the nominal resolution axially from 2·5 to 4·5 nm has only marginal effects on the 3-D structure of F-actin filament reconstructions (not shown). By contrast, reducing the nominal resolution from 2·5 to 4·5 radially (not shown) or isotropically (see Figure 6c, top panel) produces a transition from intersubunit contacts along and between the two long-pitch helical strands to predominant contact along the left-handed genetic helix. Egelman and co-workers (Orlova & Egelman, 1992, 1993) have compared their 3-D reconstructions with electron density maps computed from atomic models of the actin filament based on Holmes *et al.* (1990) and observed good overall similarity except for subdomain 2: in this area their reconstructions revealed less mass than the atomic model, thus confirming our previous notion that in F-actin subdomain 2 may be disordered (Bremer *et al.*, 1991) or in a conformation distinct from that of actin in the actin-DNase I crystal (Bremer & Aebi, 1992; and see above). Furthermore, the intersubunit bonding patterns revealed in the various 3-D reconstructions presented by Egelman and co-workers (Orlova & Egelman, 1992, 1993) differed significantly from those of their surface-rendered electron density maps calculated from the atomic model presented by Holmes and co-workers (Holmes *et al.*, 1990) and variations thereof. To put the biological significance of these apparent structural differences in perspective, it should be stressed that the different F-actin filament 3-D reconstructions presented by Orlova & Egelman (1992, 1993) have a comparable axial resolution but a lower effective radial resolution than the computed electron density maps. In other words, the limited radial resolution of their EM data, rather than conformational differences, may be the primary reason for the differences that Orlova & Egelman (1992) observed between their 3-D reconstructions and computed electron density maps.

Drs Wolfgang Kabsch, Ken Holmes and Michael Lorenz kindly provided the coordinates of the atomic structure of the actin molecule as well as the atomic coordinates of their F-actin filament models. This work was supported by the

M. E. Müller Foundation of Switzerland, research grants of the Swiss National Science Foundation (31-30129·90 to U.A., and 31-32536·91 to A.E.), and a grant from Silicon Graphics Inc. A.B. received fellowships of the Studienstiftung des Deutschen Volkes, Germany, and the International Human Frontier Science Program Organization, Strasbourg, France (LT-381/93). Development of the MDPP micrograph data processing program package was supported in part by the US National Science Foundation.

References

Aebi, U., Millonig, R., Salvo, H. & Engel, A. (1986). The three-dimensional structure of the actin filament revisited. *Ann. N.Y. Acad. Sci.* **483**, 100–119.

Bray, D. (1992). *Cell Movements*. Garland Publishing, New York and London.

Bremer, A. & Aebi, U. (1992). The structure of the F-actin filament and the actin molecule. *Curr. Opin. Cell Biol.* **4**, 20–26.

Bremer, A. & Aebi, U. (1994). Negative staining. In *Cell Biology: A Laboratory Handbook* (Celis, J. E., ed.), In the press.

Bremer, A., Millonig, R. C., Sütterlin, R., Engel, A., Pollard, T. D. & Aebi, U. (1991). The structural basis for the intrinsic disorder of the F-actin filament: the lateral slipping model. *J. Cell Biol.* **115**, 689–703.

Bremer, A., Henn, C., Engel, A., Baumeister, W. & Aebi, U. (1992). Has negative staining still a place in biomacromolecular electron microscopy? *Ultramicroscopy*, **46**, 85–111.

Bullit, E. S. A., DeRosier, D. J., Coluccio, L. M. & Tilney, L. G. (1988). Three-dimensional reconstruction of an actin bundle. *J. Cell Biol.* **107**, 507–611.

Carlier, M. F. (1991). Nucleotide hydrolysis in cytoskeletal assembly. *Curr. Opin. Cell Biol.* **3**, 12–17.

Carson, M. (1987). Ribbon models of macromolecules. *J. Mol. Graph.* **5**, 103–106.

Censullo, R. & Cheung. H. C. (1993). A rotational offset model for two-stranded F-actin. *J. Struct. Biol.* **110**, 75–83.

Chen, X., Cook, R. K. & Rubenstein, P. A. (1993). Yeast actin with a mutation in the 'hydrophobic plug' between subdomains 3 and 4 ($L_{266}D$) displays a cold-sensitive polymerization defect. *J. Cell Biol.* **123**, 1185–1195.

Cowan, S. W., Schirmer, T., Rummel, G., Steiert, M., Ghosh, R., Pauptit, R., Jansonius, J. N. & Rosenbusch, J. (1992). Crystal structures explain functional properties of two *E. coli* porins. *Nature (London)*, **358**, 727–733.

DeRosier, D. & Moore, P. B. (1970). Reconstruction of three-dimensional images from electron micrographs of structures with helical symmetry. *J. Mol. Biol.* **52**, 355–369.

Engel, A., Hoenger, A., Hefti, A., Henn, C., Ford, R. C., Kistler, J. & Zulauf, M. (1992). Assembly of 2-D membrane protein crystals: dynamics, crystal order, and fidelity of structure analysis by electron microscopy. *J. Struct. Biol.* **109**, 219–234.

Erickson, H. P. (1989). Co-operativity in protein-protein association. The structure and stability of the actin filament. *J. Mol. Biol.* **206**, 465–474.

Herman, I. M. (1993). Actin isoforms. *Curr. Opin. Cell Biol.* **5**, 48–55.

Holmes, K. C. & Kabsch, W. (1991). Muscle proteins: actin. *Curr. Opin. Struct. Biol.* **1**, 270–280.

Holmes, K. C., Popp, D., Gebhard, W. & Kabsch, W. (1990). Atomic model of the actin filament. *Nature (London)*, **347**, 44–49.

Holmes, K. C., Sander, C. & Valencia, A. (1993). A new ATP-binding fold in actin, hexokinase and HSC70. *Trends Cell Biol.* **3**, 53–59.

Janmey, P. A., Hvidt, S., Oster, G. F., Lamb, J., Stossel, T. P. & Hartwig, J. H. (1990). Effect of ATP on actin filament stiffness. *Nature (London)*, **347**, 95–99.

Jeng, T.-W., Crowther, R. A., Stubbs, G. & Chiu, W. (1989). Visualization of alpha-helices in tobacco mosaic virus by cryo-electron microscopy. *J. Mol. Biol.* **205**, 251–257.

Kabsch, W. & Vandekerckhove, J. (1992). Structure and function of actin. *Annu. Rev. Biophys. Biomol. Struct.* **21**, 49–76.

Kabsch, W., Mannherz, H. G., Suck, D., Pai, E. & Holmes, K. C. (1990). Atomic structure of the actin:DNase I complex. *Nature (London)*, **347**, 37–44.

Klug, A. D. & DeRosier, D. J. (1966). Optical filtering of electron micrographs: reconstruction of one-sided images. *Nature (London)*, **212**, 29–32.

Lepault, J., Erk, I., Nicolas, G. & Ranck, J.-L. (1991). Time-resolved cryo-electron microscopy of vitrified muscular components. *J. Microsc.* **161**, 47–57.

Lepault, J., Ranck, J.-L., Erk, I. & Carlier, M.-F. (1994). Small angle X-ray scattering and electron cryo-microscopy study of actin filaments: role of the bound nucleotide in the structure of F-actin. *J. Struct. Biol.* **112**, 79–91.

Lorenz, M., Popp, D. & Holmes, K. C. (1993). Refinement of the F-actin model against X-ray fiber diffraction data by the use of a directed mutation algorithm. *J. Mol. Biol.* **234**, 826–836.

Lorenzen, W. E. & Cline, H. E. (1987). Marching cubes: a high resolution surface construction algorithm. *Comput. Graph.* **21**, 163–169.

McLaughlin, P. J., Gooch, J. T., Mannherz, H.-G. & Weeds, A. G. (1993). Structure of gelsolin segment 1-actin complex and the mechanism of filament severing. *Nature (London)*, **364**, 685–692.

Milligan, R. A. & Flicker, P. F. (1987). Structural relationships of actin, myosin, and tropomyosin revealed by cryo-electron microscopy. *J. Cell Biol.* **105**, 29–39.

Milligan, R. A., Whittaker, M. & Safer, D. (1990). Molecular structure of F-actin and location of surface binding sites. *Nature (London)*, **348**, 217–221.

Millonig, R. C., Salvo, H. & Aebi, U. (1988). Probing actin polymerization by intermolecular cross-linking. *J. Cell Biol.* **106**, 785–796.

Moore, P. B., Huxley, H. E. & DeRosier, D. J. (1970). Three-dimensional reconstruction of F-actin, thin filaments and decorated thin filaments. *J. Mol. Biol.* **50**, 279–295.

Müller, S. A., Goldie, K. N., Bürki, R., Häring, R. & Engel, A. (1992). Factors influencing the precision of quantitative scanning transmission electron microscopy. *Ultramicroscopy*, **46**, 317–334.

Namba, K. & Stubbs, G. (1986). Structure of tobacco mosaic virus at 3·6 Å resolution: implications for assembly. *Science*, **231**, 1401–1406.

Oosawa, F. & Kasai, M. (1962). A theory of linear and helical aggregation of macromolecules. *J. Mol. Biol.* **4**, 10–21.

Orlova, A. & Egelman, E. H. (1992). Structural basis for the destabilization of F-actin by phosphate release following ATP-hydrolysis. *J. Mol. Biol.* **227**, 1043–1053.

Orlova, A. & Egelman, E. H. (1993). A conformational change in the actin subunit can change the flexibility of the actin filament. *J. Mol. Biol.* **232**, 334–341.

Owen, C. & DeRosier, D. (1993). A 13-Å map of the actin-scruin filament from the Limulus acrosomal process. *J. Cell Biol.* **123**, 337–344.

Pollard, T. D. (1990). Actin. *Curr. Opin. Cell Biol.* **2**, 33–40.

Popp, D., Lednev, V. V. & Jahn, W. (1987). Methods for preparing well-oriented sols of F-actin containing filaments suitable for X-ray diffraction. *J. Mol. Biol.* **197**, 679–684.

Rayment, I., Rypniewski, W. R., Schmidt-Bäse, K., Smith, R., Tomchick, D. R., Benning, M. M., Winkelmann, D. A., Wesenberg, G. & Holden, H. M. (1993*a*). Three-dimensional structure of myosin subfragment-1: a molecular motor. *Science*, **261**, 50–58.

Rayment, I., Holden, H. M., Whittaker, M., Yohn, C. B., Lorenz, M., Holmes, K. C. & Milligan, R. A. (1993*b*). Structure of the actin-myosin complex and its implications for muscle contraction. *Science*, **261**, 58–65.

Reisler, E. (1993). Actin molecular structure and function. *Curr. Opin. Cell Biol.* **5**, 41–47.

Saxton, O. W. & Baumeister, W. (1982). The correlation averaging of a regularly arranged bacterial cell envelope protein. *J. Microsc.* **127**, 127–138.

Schmid, M. F., Agris, J. M., Jakana, J., Matsudaira, P. & Chiu, W. (1994). Three-dimensional structure of a single filament in the *Limulus* acrosomal bundle: scruin binds to homologous helix-loop-beta motifs in actin. *J. Cell Biol.* **124**, 341–350.

Schröder, R. R., Manstein, D. J., Jahn, W., Holden, H., Rayment, I., Homes, K. C. & Spudich, J. A. (1993). Three-dimensional atomic model of F-actin decorated with *Dictyostelium* myosin S1. *Nature (London)*, **364**, 171–174.

Schutt, C. E., Myslik, J. C., Rozycki, M. D., Goonesekere, N. C. W. & Lindberg, U. (1993). The structure of crystalline profilin-β-actin. *Nature (London)*, **365**, 810–816.

Smith, P. R. (1978). An integrated set of computer programs for processing electron micrographs of biological structures. *Ultramicroscopy*, **3**, 153–160.

Smith, P. R. & Aebi, U. (1974). Computer generated Fourier transforms of helical particles. *J. Phys. A: Gen. Phys.* **7**, 1627–1633.

Smith, P. R., Aebi, U., Josephs, R. & Kessel, M. (1976). Studies on the structure of the bacteriophage T4 tail sheath. I. The recovery of 3-D structural information from the extended sheath. *J. Mol. Biol.* **106**, 243–271.

Squire, J. M., Al-Khayat, H. A. & Yagi, N. (1993). Muscle thin-filament structure and regulation. *J. Chem. Soc. Faraday Trans.* **89**, 2717–2726.

Stewart, M. (1988). Computer image processing of electron micrographs of biological structures with helical symmetry. *J. Electron Microsc. Tech.* **9**, 325–358.

Taylor, K. A. & Amos, L. A. (1981). A new model for the geometry of the binding of myosin cross-bridges to muscle thin filaments. *J. Mol. Biol.* **147**, 297–324.

Tirion, M. M. & ben-Avraham, D. (1993). Normal mode analysis of G-actin. *J. Mol. Biol.* **230**, 186–195.

Trinick, J., Cooper, J., Seymour, J. & Egelman, E. H. (1986). Cryo-electron microscopy and three-dimensional reconstruction of actin filaments. *J. Microsc.* **141**, 349–360.

Unwin, P. N. T. & Klug, A. (1974). Electron microscopy of the stacked disk aggregate of tobacco mosaic virus protein. I. Three-dimensional reconstruction. *J. Mol. Biol.* **87**, 641–656.

Vibert, P., Craig, R. & Lehmann, W. (1993). Three-dimensional reconstruction of caldesmon-containing smooth muscle thin filaments. *J. Cell Biol.* **123**, 313–321.

Edited by R. Huber

(Received 5 April 1994; accepted 21 June 1994)